Article

Infrared nanosensors of piconewton to micronewton forces

https://doi.org/10.1038/s41586-024-08221-2

Received: 25 October 2023

Accepted: 15 October 2024

Published online: 1 January 2025

Check for updates

Natalie Fardian-Melamed[1]✉, Artiom Skripka[2,3,6], Benedikt Ursprung[1], Changhwan Lee[1], Thomas P. Darlington[1], Ayelet Teitelboim[2], Xiao Qi[2], Maoji Wang[4], Jordan M. Gerton[4], Bruce E. Cohen[2,5]✉, Emory M. Chan[2]✉ & P. James Schuck[1]✉

Mechanical force is an essential feature for many physical and biological processes[1–7], and remote measurement of mechanical signals with high sensitivity and spatial resolution is needed for diverse applications, including robotics[8], biophysics[9,10], energy storage[11] and medicine[12,13]. Nanoscale luminescent force sensors excel at measuring piconewton forces, whereas larger sensors have proven powerful in probing micronewton forces[14–16]. However, large gaps remain in the force magnitudes that can be probed remotely from subsurface or interfacial sites, and no individual, non-invasive sensor is capable of measuring over the large dynamic range needed to understand many systems[14,17]. Here we demonstrate Tm^{3+}-doped avalanching-nanoparticle[18] force sensors that can be addressed remotely by deeply penetrating near-infrared light and can detect piconewton to micronewton forces with a dynamic range spanning more than four orders of magnitude. Using atomic force microscopy coupled with single-nanoparticle optical spectroscopy, we characterize the mechanical sensitivity of the photon-avalanching process and reveal its exceptional force responsiveness. By manipulating the Tm^{3+} concentrations and energy transfer within the nanosensors, we demonstrate different optical force-sensing modalities, including mechanobrightening and mechanochromism. The adaptability of these nanoscale optical force sensors, along with their multiscale-sensing capability, enable operation in the dynamic and versatile environments present in real-world, complex structures spanning biological organisms to nanoelectromechanical systems.

Engineered and biological systems, such as integrated nanoelectromechanical systems, developing embryos, energy storage units and migrating cells, experience multiple scales of force as a consequence of their inherently complex, multicomponent designs that span disparate length scales[5,9,11,19–24]. The ability to study force-dependent processes in such systems is essential for understanding their central mechanisms[25,26]. Remotely addressable probes are needed for in situ detection of changes or malfunction in these processes, particularly below surfaces or at nanoscale interfaces[13,22,27,28]. At such interfaces, environmental constraints or sample fragility render direct force measurements and electrical data transmission impractical or impossible.

Optical methods excel at minimally invasive mechanical sensing and can detect force-induced displacements with exquisite sensitivity[10,14,29]. However, their spatial resolutions are limited by the diffraction limit[10,14,29]. Single luminescent nanoprobes may act as reporters of local forces, but with limited dynamic ranges[14,17], so that no single probe is capable of measuring the range of forces existing in complex systems (Fig. 1a). Although luminescent force sensors have proven useful in understanding the molecular forces within cells[14], challenges remain with limited photostability (restricting continuous force monitoring) and reliance on visible wavelengths (inhibiting subsurface or deep-tissue measurements).

To develop a stable, near-infrared force-sensing system with a large dynamic range, we took advantage of unexpected observations that avalanching nanoparticles (ANPs) undergo significant changes in emission when tapped with atomic force microscopy (AFM) tips. ANPs[18,30–34] are a class of steeply nonlinear upconverting nanoparticles (UCNPs), which are lanthanide-based nanocrystal phosphors that convert multiple sequentially absorbed near-infrared photons into higher-energy emitted photons, and show no overlap with sample autofluorescence, no on–off blinking and no measurable photobleaching, even under prolonged lasing or single-particle excitation[35–40]. Calculations show that ANP quantum yields can reach 45% (of 50%, for 2-photon upconversion)[18], and like other shelled UCNPs, they are efficiently excited with continuous-wave excitation[18,39], and can be imaged with no measurable background[35] and with little or no sensitivity to ambient chemicals[41]. Because of their steeply nonlinear relation between pump power and emission intensity, ANPs are able to amplify minute changes in signal input to giant changes in output (that is, $I_{out} = I_{in}^{s}$; where I is intensity and nonlinear order $s > 10$)[18,30–34]. Recent studies have shown that both

[1]Department of Mechanical Engineering, Columbia University, New York, NY, USA. [2]The Molecular Foundry, Lawrence Berkeley National Laboratory, Berkeley, CA, USA. [3]Nanomaterials for Bioimaging Group, Departamento de Física de Materiales, Facultad de Ciencias, Universidad Autónoma de Madrid, Madrid, Spain. [4]Department of Physics and Astronomy, University of Utah, Salt Lake City, UT, USA. [5]Division of Molecular Biophysics and Integrated Bioimaging, Lawrence Berkeley National Laboratory, Berkeley, CA, USA. [6]Present address: Department of Chemistry, Oregon State University, Corvallis, OR, USA. ✉e-mail: natalie.melamed@columbia.edu; becohen@lbl.gov; emchan@lbl.gov; p.j.schuck@columbia.edu

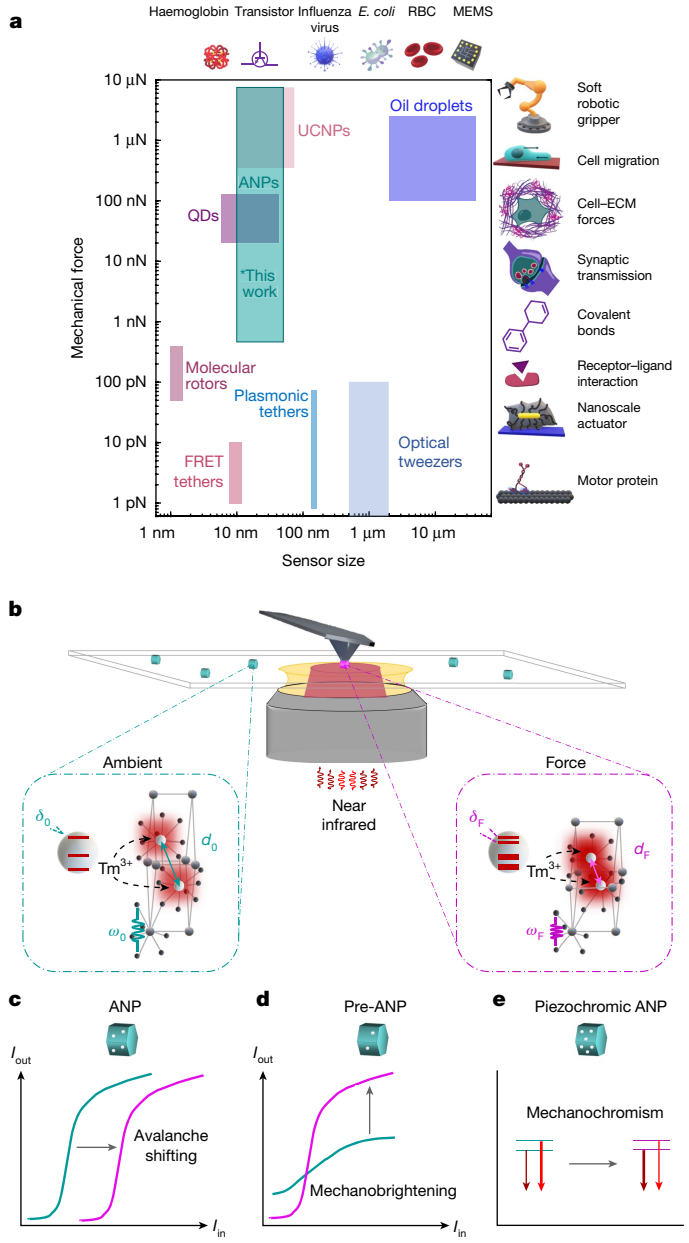

Fig. 1 | Photon-avalanche-based nanoscale force sensors. a, Comparison of force dynamic range and sensor size with previously reported[14,15,17,49] luminescent force sensors. QD, semiconductor quantum dot; FRET, Förster resonance energy transfer; RBC, red blood cell; MEMS, microelectromechanical systems; ECM, extracellular matrix. **b**, A combination of changes in electronic level positions and splittings (δ), interionic distance (d) and vibrational mode energy ($\hbar\omega$) within a Tm^{3+}-doped $NaYF_4$ nanoparticle under applied force leads to three optical readout modalities (depicted in **c**–**e**), depending on the intrinsic Tm^{3+}-doping concentration. Subscripts 0 and F refer to initial (no force applied) and final (after force is applied) states, respectively. Light grey balls surrounded by red shading represent optically active Tm^{3+} ions. $\hbar$, reduced Planck constant; ω, vibrational mode angular frequency. **c**, Moderately doped (4.5–8% Tm^{3+}) ANPs show steeply nonlinear emission versus excitation curves that shift with applied force, enabling observation of large emission signal change with minute applied force. **d**, Lower-doped (4% Tm^{3+}) pre-ANPs transform from their energy-looping state to an avalanching state, prompting substantial emission enhancement with applied force. **e**, Highly doped (15% Tm^{3+}) piezochromic ANPs emit light from two Tm^{3+} energy levels with intensities that vary differently under applied force, enabling ratiometric optical readout of applied force.

the photon-avalanche threshold and the degree of nonlinearity s can be modified by manipulating the lanthanide concentration[18,30,31].

To determine the mechano-optical response of thulium (Tm^{3+})-doped sodium yttrium fluoride ($NaYF_4$) ANPs, we studied them as single ANPs under ambient conditions, using AFM tips for force application, in combination with an inverted optical microscope for near-infrared excitation and emission measurements (Fig. 1b). To minimize quenching or energy transfer between the ANPs and the tip or other surrounding components[42,43], we synthesized all ANPs in this study with thick (>5 nm) undoped $NaYF_4$ shells (Supplementary Note 1, Supplementary Table 1 and Supplementary Fig. 1).

ANPs access a wide dynamic range of forces

The photon-avalanching process and the lowest laser intensity at which a photon avalanche is observed depend on several factors, including the ANP Tm^{3+} concentration, the vibrational energy modes of the ANP material, and the influence of crystal field symmetries on Tm^{3+} electronic energy levels[18,30,31,44,45]. We considered that such factors could be sensitive to force. For example, compressive force should slightly decrease the interionic distances within the ANP, possibly affecting energy transfer rates (Supplementary Notes 2 and 3, and Supplementary Figs. 2–4). It could also increase the energy of the ANP vibrational modes and hence the non-radiative rates[46–48] (Supplementary Notes 4 and 5), which would shift the avalanche onset to higher excitation intensities[18] (as in Fig. 1c). To test this hypothesis, we measured the emission intensity versus excitation fluence for a single ANP, with and without applied force (Fig. 2a). We find that the excitation–emission curve measured at an applied force as low as 200 nN is markedly shifted from the one measured without applying force; the same emission intensity measured at ambient force is acquired at an excitation intensity 62% larger when 200 nN is applied to the ANP.

The marked shift of the ANP excitation–emission curve with force implies that a large change in ANP emission will be observed per unit force for a given pump power, offering high mechano-optical sensitivity. To quantify the response, we measured the force-dependent optical emission for a series of forces, at a constant pump power. We repeated this measurement for different pump powers, in the avalanching regime (where the degree of nonlinearity $s > 10$) and in the saturation regime (where $s \approx 2$) of the single ANPs (Fig. 2b and Extended Data Figs. 1 and 2). We find that the mechano-optical response of an ANP is exceptionally large for all pump powers, enabling the detection of 620-pN forces in the avalanching regime and single-digit nanonewton forces in the saturation regime (Fig. 2c,d, Supplementary Note 7 and Methods).

To determine the dynamic range of forces measurable with an ANP, we applied 0 to 2.5-µN forces upon each ANP, and optically measured the lowest and highest detectable forces. The lowest detectable force, namely, the noise-defined resolution, is shot-noise-limited and is fundamentally dependent on the noise-equivalent sensitivity (NES)[49,50] of the ANP—a figure of merit corresponding to the smallest detectable change in signal over a 1-s integration (Methods and Supplementary Note 7). We detect 620 pN within 3 s, and the NES of an ANP may reach 480 pN $Hz^{-1/2}$ within the avalanching regime of the ANP (Fig. 2c, Extended Data Fig. 1b,c, Supplementary Fig. 8, and Supplementary Notes 7 and 8). The highest detectable force, namely, the force range, is dark-noise limited and is fundamentally dependent on the intrinsic quantum yield of the ANP and the nanocrystal elastic limit (Supplementary Note 8). We detect 1.7 µN of force within the saturation regime of these ANP compositions. We observe no optical degradation resulting from plastic deformation or photobleaching, for up to 25 compression cycles (the maximum number of cycles attempted) measured within this 2.5-µN force range and these measurement times and pump powers (Supplementary

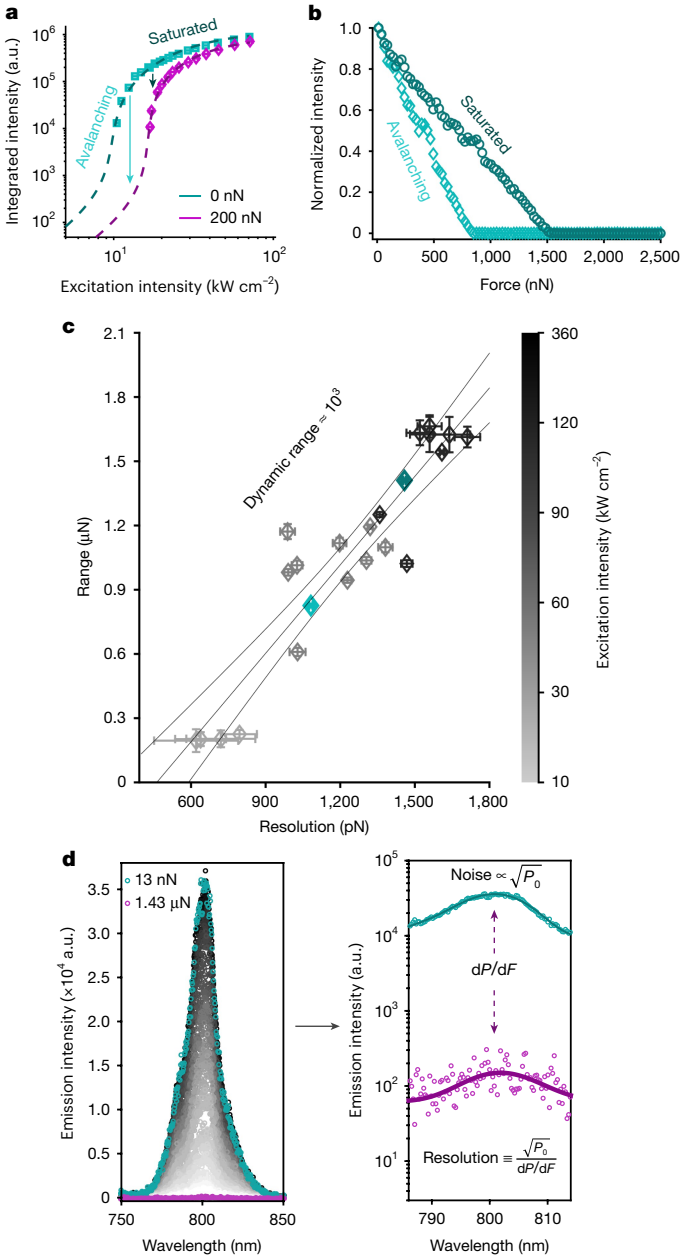

Fig. 2 | Optical force sensing over four orders of magnitude by a single ANP. **a**, Emission (800 nm) versus excitation (1,064 nm) intensities measured for a single 4.5% Tm^{3+} ANP, with and without applied force. The dashed lines are photon-avalanche differential rate equation model fits (Supplementary Note 6 and Supplementary Tables 2 and 3). The larger (smaller) change in signal per unit force, represented by the left (right) arrow, occurs in the avalanching (saturation) regime of the ANP. **b**, Emission intensity as a function of applied force for a single 7% Tm^{3+} ANP excited at avalanching and saturating intensities. **c**, Highest detectable force (range) and lowest detectable force (resolution) for 23 compression cycles for 7 single 7% Tm^{3+} ANPs measured at different excitation intensities. Standard errors of the mean are derived from the linear fits to the emission intensity versus applied force graphs (as in **b**), each containing 10–200 data points. Both compression cycles from the single ANP in **b** are enlarged and colour-coded as in **b**. **d**, Emission spectra (left) and their peak magnifications (right) measured at the start and end of a compression cycle, for a 7% Tm^{3+} ANP excited at saturating intensities. Left: 30 force-dependent spectra (grey traces) measured between 13 nN (teal) and 1.4 μN (pink) of the compression cycle. Right: log-scale representation of peaks from the 13-nN and 1.4-μN spectra in the left panel, with the equation for noise-defined resolution, where P is photon count (integrated intensity), F is force and P_0 is the photon count at $F = 0$. The 13-nN spectrum is fit to a sum of Gaussians centred at Tm^{3+} transitions ($R^2 = 0.99$). Integration times are 3 s for all measurements.

Note 8, Supplementary Fig. 8 and Extended Data Fig. 2). We find that the highly nonlinear mechano-optical response, which is maximized at the avalanching regime, enables the detection of hundreds of piconewtons to hundreds of nanonewtons forces at lower pump powers (Fig. 2c and Supplementary Note 10). Meanwhile, the ANP high emission, which is maximized at the saturation regime, allows the detection of single-digit nanonewtons to single-digit micronewtons at higher pump intensities (Fig. 2c,d). The same large dynamic range spanning three orders of magnitude of force is maintained throughout all pump intensities for all single ANPs measured (Fig. 2c), and a single ANP can detect four orders of magnitude of force by pump-power tuning.

Mechanobrightening through UCNP-to-ANP transformation

Motivated by these results, we predicted that photon-avalanching behaviour could be initiated by applied force, resulting in mechanobrightening nanosensors. We envisioned creating non-avalanching UCNPs with Tm^{3+} concentrations just below those sufficient to attain photon avalanche at ambient conditions, and transforming them into avalanching UCNPs through the utilization of force.

It was previously found that ANPs with 8% Tm^{3+} show a signature photon-avalanching response[18]. But for lower concentrations of 1% to 4%, a threshold intensity was less apparent, and the nonlinearities observed in the emission versus excitation curves were much smaller[18]. As photon avalanching is sustained through efficient cross-relaxation (a form of energy transfer) between the emitting lanthanides[18], which is influenced by interionic distances, phonon-mediated processes and excited-state absorptions, we posited that application of force could enhance this process, and hence transform a pre-avalanching nanoparticle (pre-ANP) into an ANP. We therefore designed a set of particles with Tm^{3+} concentrations ranging from 7% to 4%, in search of the pre-avalanching concentration. We find that when pressing upon particles with Tm^{3+} concentrations down to 4.5%, the emission decreases with applied force. In addition, 4.5% Tm^{3+} nanoparticles show steeply nonlinear emission versus excitation (Fig. 2a, Supplementary Fig. 5b and Supplementary Table 3), deeming them ANPs at ambient conditions. However, when pressing upon 4% Tm^{3+} nanoparticles, which do not avalanche at ambient conditions (Supplementary Figs. 5a and 6), the emission intensity increases and is enhanced 4-fold for a single force ramp of only about 400 nN (Fig. 3a).

To test the viability of mechanobrightening for force sensing, we repeatedly applied forces of 0 to 2.5 μN upon single pre-ANPs, excited at various pump powers (Extended Data Fig. 3). We find that the transformation into an ANP occurs at around 400 nN, after which the now-ANP follows conventional ANP response to force—that of emission decrease. This yields a mechanobrightening force range of about 400 nN for pre-ANPs. The steep increase in emission per unit force enables the detection of forces as low as 475 pN within 3 s (Fig. 3a, inset), yielding an NES of 368 pN $Hz^{-1/2}$ for pre-ANPs (Supplementary Notes 7, 8 and 10, and Methods). The ability to detect forces at such high sensitivities, over wide ranges, with an amplifying emission signal, along with the robustness and repeatability of the signal under continuous pumping and force application (Fig. 3b and Extended Data Fig. 3e) make pre-ANPs highly attractive for remote mechanical sensing.

To further understand how force transforms pre-ANPs into ANPs, we characterized the emission versus excitation profile of a pre-ANP with and without applied force. Unlike ANP excitation–emission curves, which shift to the right upon application of force (Figs. 1c and 2a)—pre-ANP excitation–emission curves shift upwards, with increased nonlinearity, manifested in the larger excitation–emission curve slope (Figs. 1d and 3c). This distinct change in the excitation–emission profile,

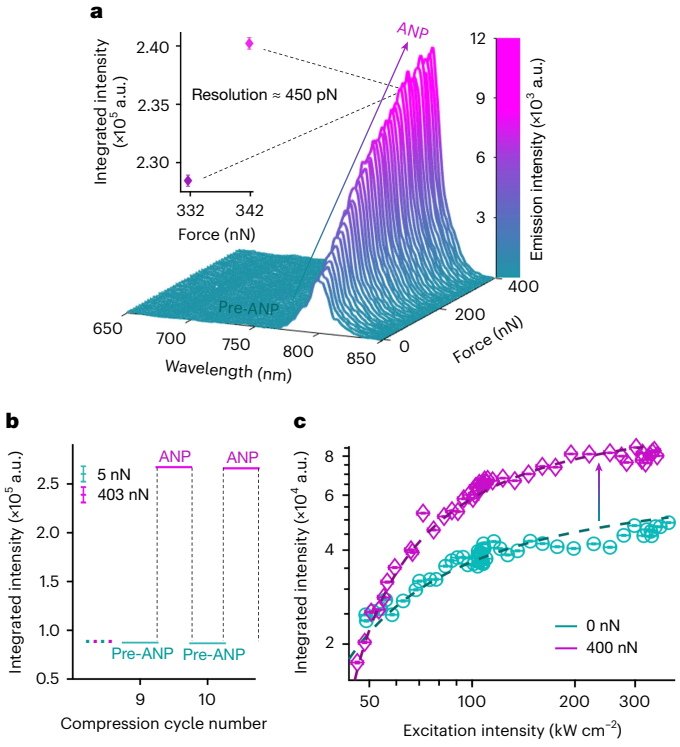

Fig. 3 | Sensitivity and cyclability of pre-ANP to ANP mechanobrightening. **a**, Emission spectra as a function of applied force for a single 4% Tm^{3+} UCNP undergoing a pre-ANP-to-ANP transition. Inset: integrated intensities from two sequentially measured emission spectra collected in 10-nN increments. Noise-defined resolution is calculated from a full force–emission compression cycle as in Fig. 2d. **b**, Integrated emission as a function of force for a single nanoparticle, after multiple compression cycles (5 nN to 403 nN applied force; each full compression cycle consists of 75 force–emission measurements and lasts 4 min), demonstrating reproducible pre-ANP-to-ANP transitions. Symbols (closely packed, so appearing as solid lines) are mean ± standard deviation. **c**, Integrated emission (at 800 nm) versus excitation (at 1,064 nm) intensities measured for a single pre-ANP with and without applied force. The dashed lines are photon-avalanche differential rate equation model fits (Supplementary Note 6 and Supplementary Tables 2 and 3). In **a**–**c**, the error bars for the excitation and emission intensities are based on excitation-area determination (±0.04 I_{in}) and signal Poissonian statistics (approximately $\sqrt{I_{out}}$), respectively. The integration time is 3 s for all measurements.

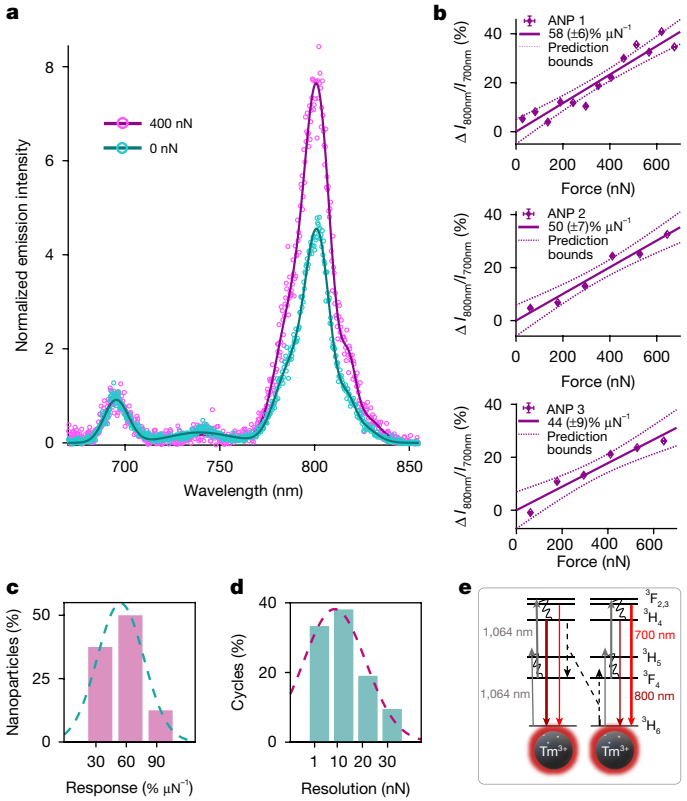

Fig. 4 | Ratiometric mechanochromism of dual-wavelength ANPs. **a**, Emission spectra collected from a single 15% Tm^{3+} piezochromic ANP with and without applied force, normalized to the $^3F_3$ (700 nm) emission peak. Spectra are fit to sums of Gaussian functions centred at Tm^{3+} transitions ($R^2 = 0.99$ for both spectra). **b**, Change in the ratio of 800-nm to 700-nm emission versus applied force, for 3 compression cycles originating from 3 different piezochromic ANPs. The dashed lines represent the 95% confidence intervals of the linear fits. The integration times are 50 s (ANP 1), 20 s (ANP 2) and 30 s (ANP 3). **c**, Mechano-optical response distribution (response, 54 ± 7% μN^{-1}; data, mean ± s.e.m.). **d**, Force resolution distribution (resolution, 13 ± 2 nN; data, mean ± s.e.m.). The data in **c** and **d** are derived from 21 compression cycles (each consisting of 10–1,000 emission versus force data points) on 8 piezochromic ANPs. The integration times are 3–50 s. The dashed lines are Gaussian fits to the histograms. **e**, The main Tm^{3+} electronic levels and transitions involved when considering piezochromic dual-wavelength emission. The solid lines are absorption and emission. The wavy and dashed lines represent multi-phonon relaxation and cross-relaxation, respectively.

observed only for pre-ANPs under applied force, highlights their transition from pre-avalanching to avalanching (Supplementary Note 6 and Supplementary Fig. 5).

Mechanochromic nanosensors

With a goal of expanding utility for a broader range of applications, we next set out to design mechanochromic nanosensors, with a dual-wavelength ratiometric readout of force. The aim was a sensor for which the signal does not depend solely on the intensity of one emission wavelength, but instead on the intensity of two emission wavelengths that each show a different force response. The wavelengths should be spectrally proximal to enable their simultaneous detection, yet far enough apart to not overlap, yielding a force-dependent signal that depends on the ratio of these two emissions (the 'colour' of emission). Mechanochromic self-calibrated signals of this type provide a built-in control against environmental interference, which can disrupt single-wavelength intensity readout. The internal calibration provided by mechanochromism makes it well suited for deeply subsurface mechanical sensing.

To design mechanochromic nanosensors with substantial emission from both the main photon-avalanche level ($^3H_4$) and a nearby energy level ($^3F_3$), we increased the Tm^{3+} concentration within the ANPs. We find that for 15% Tm^{3+}, there is sizeable emission at 700 nm ($^3F_3$ level) and 800 nm ($^3H_4$ level) (Fig. 4a and Extended Data Fig. 4) and hereafter refer to 15% Tm^{3+} nanoparticles as 'piezochromic ANPs'.

When subjected to force, the relative emission from the $^3H_4$ level increases compared with that from the $^3F_3$ level (Fig. 4a), and the overall emission from a piezochromic ANP decreases with force (Extended Data Fig. 5a) as with the lower-Tm^{3+}-content ANPs (Fig. 2). The ratio between these two emission lines, therefore, reports on the applied force. The mechano-optical response, manifested in the percent change of the 800 nm/700 nm emission ratio per unit force, is the same within error for different single particles probed during different integration times (Fig. 4b and Extended Data Figs. 5b–f and 7a,b), and is on average 54% μN^{-1} (Fig. 4c). For each piezochromic ANP, the response, ambient-force brightness and ambient-force dual-emission ratio remain unchanged under continuous pumping at high excitation intensities and after repeated compression to 2.5 μN

(Extended Data Figs. 6 and 9a–d). The large mechano-optical response and ambient-force brightness, together with the low ambient-force dual-emission ratio found for piezochromic ANPs (Extended Data Figs. 6, 8 and 9a–d) enable the detection of single-digit nanonewton forces within less than 1 min (Fig. 4d and Extended Data Fig. 9e), and yield an NES of 6.8 nN $Hz^{-1/2}$ (Supplementary Notes 7 and 8 and Extended Data Fig. 8).

Discussion

The steep nonlinearity of the photon-avalanche process in addition to the high intrinsic quantum yield of ANPs[18] enables the detection of three orders of magnitude of force at any pump intensity utilized. Overall, we demonstrate that four or more orders of magnitude of force can be probed with the same single ANP by simply adjusting the pump intensity—allowing for remote multiple-scale force sensing of nanoscale environments. While many experimental measures of force are macroscopic or ensemble measurements[14,17,49,50], we have carried out single-ANP experiments here, allowing for quantitative characterization of ANP responses, and for precise control of applied forces over many orders of magnitude with an AFM tip. Single-ANP studies can be useful for applications needing deeply subwavelength spatial mapping[18] or tracking of force variations. Innate nanoparticle variations[51,52] will present a limiting factor on quantitative precision in such studies and will be a key aspect for future optimization (Supplementary Note 9 and Supplementary Figs. 9–12). As with many remote sensors, sensitivity to other external factors such as temperature can also present issues[44]. New ANP architectures[34,53] may address this challenge, offering the potential for self-calibration using other lanthanide species or ratiometric detection to independently track and disentangle confounding external effects.

The ability to transform a conventional UCNP into an ANP and back through the application and release of force, respectively, further highlights the strong dependence of the photon-avalanche mechanism on factors such as interionic distance, phonon energy and electronic energy-level splittings and symmetries. Only 400 nN of force are required to observe a 4-fold emission increase at ambient conditions. Although emission intensity increase with pressure has been shown in previous hydrostatic pressure studies of lanthanide-doped UCNPs[46,54], an enhancement of 1.7-fold was observed at most, using orders of magnitude larger forces. Those changes in signal were attributed to modifications of the crystal field symmetry, as the nanoparticles under study were of cubic phase, and hence centro-symmetric in nature. Compression of hexagonal-phase nanoparticles in those studies did not yield a measurable increase in signal with pressure. Because the pre-ANPs in this study are hexagonal-phase nanoparticles, we speculate that the observed changes rely on the complex, photon-avalanche-related interactions. Analysis of the experimental data using an extended differential rate equation model including all Tm^{3+} levels involved in 800-nm avalanche emission (Supplementary Note 6) results in accurate fits for the mechano-optics of all Tm^{3+} concentrations in this study (Supplementary Tables 2 and 3, Supplementary Fig. 5 and Extended Data Fig. 7c). These show increases in non-radiative relaxation and cross-relaxation rates upon force application that are consistent with expected changes in phonon energies and interionic distances (Supplementary Notes 3–5), pointing towards the primary mechanisms responsible for the force-induced transition to avalanching, that results in the mechanobrightening and detection of the wide range of forces (475 pN to 400 nN) observed here.

The piezochromic ANPs designed here are an order of magnitude more sensitive than the state-of-the-art nanoscale ratiometric force sensors at ambient conditions[49,50]. However, piconewton-scale forces, easily detectable with pre-ANPs and ANPs, were not detected with piezochromic ANPs with the same experimental conditions (Extended Data Fig. 10). This contrasting behaviour could originate from different or additional underlying mechanisms behind the mechanochromism ratiometric change. Concentration-dependent measurements (Extended Data Fig. 4a,b) and modelling (Extended Data Fig. 4c) indicate that the emergence of 700-nm emission from the $^3F_3$ level arises from the increased cross-relaxation rates present in high-lanthanide-content nanoparticles owing to shorter average interionic distances. Our models suggest that the force sensitivity in piezochromic ANPs could then stem from an increase in the non-radiative relaxation rate between the $^3F_3$ level and the $^3H_4$ level (Supplementary Fig. 7) resulting from an increase in the vibrational energy of the host lattice upon applied force, as seen in previous studies of lanthanide-doped $NaYF_4$ (refs. 46,47,55).

Directional compressive forces are prevalent in many phenomena and processes ranging from synaptic transmission[2] to robotic tactility[56] to cell migration and differentiation[19–21]. Photon-avalanche-based sensors facilitate the remote detection of such forces from nanoscale environments. As the ANPs undergoing axial compression also undergo orthogonal expansion owing to the Poisson effect (Supplementary Note 2), the avalanche-related observations in this study may be further amplified under other conditions such as hydrostatic pressure. A dedicated study of nano-confined photon avalanche under different forms of mechanical force, such as hydrostatic or tensile force, will benefit applications where these forces are the more predominant ones.

To conclude, by leveraging the high nonlinearities of photon avalanches, we design nanoscale, remotely controlled, near-infrared-input, near-infrared-output, high-dynamic-range force sensors with force sensitivities falling within previously inaccessible force ranges of existing optical nanosensors[14,49]. Different modalities of readout (from mechanobrightening to mechanochromism), with different force resolutions (from piconewtons to nanonewtons), can be utilized by choice of nanosensor Tm^{3+} concentration. The ability to remotely and accurately probe local forces on these multiple scales will enable advances in both fundamental investigations and critical applications, allowing discovery and precision study of local mechano-induced processes and, ultimately, their quantification, nano-mapping of spatial distributions, and early detection of malfunction, in technological devices and physiology.

Online content

Any methods, additional references, Nature Portfolio reporting summaries, source data, extended data, supplementary information, acknowledgements, peer review information; details of author contributions and competing interests; and statements of data and code availability are available at https://doi.org/10.1038/s41586-024-08221-2.

1. Gouveia, B. et al. Capillary forces generated by biomolecular condensates. *Nature* **609**, 255–264 (2022).
2. Ucar, H. et al. Mechanical actions of dendritic-spine enlargement on presynaptic exocytosis. *Nature* **600**, 686–689 (2021).
3. Handler, A. & Ginty, D. D. The mechanosensory neurons of touch and their mechanisms of activation. *Nat. Rev. Neurosci.* **22**, 521–537 (2021).
4. Qiu, X. & Müller, U. Sensing sound: cellular specializations and molecular force sensors. *Neuron* **110**, 3667–3687 (2022).
5. Vining, K. H. & Mooney, D. J. Mechanical forces direct stem cell behaviour in development and regeneration. *Nat. Rev. Mol. Cell Biol.* **18**, 728–742 (2017).
6. Murthy, S. E., Dubin, A. E. & Patapoutian, A. Piezos thrive under pressure: mechanically activated ion channels in health and disease. *Nat. Rev. Mol. Cell Biol.* **18**, 771–783 (2017).
7. Zeng, W.-Z. et al. Piezos mediate neuronal sensing of blood pressure and the baroreceptor reflex. *Science* **362**, 464–467 (2018).
8. Li, M., Pal, A., Aghakhani, A., Pena-Francesch, A. & Sitti, M. Soft actuators for real-world applications. *Nat. Rev. Mater.* **7**, 235–249 (2022).
9. Saraswathibhatla, A., Indana, D. & Chaudhuri, O. Cell–extracellular matrix mechanotransduction in 3D. *Nat. Rev. Mol. Cell Biol.* **24**, 495–516 (2023).
10. Gómez-González, M., Latorre, E., Arroyo, M. & Trepat, X. Measuring mechanical stress in living tissues. *Nat. Rev. Phys.* **2**, 300–317 (2020).
11. de Vasconcelos, L. S. et al. Chemomechanics of rechargeable batteries: status, theories, and perspectives. *Chem. Rev.* **122**, 13043–13107 (2022).
12. Chen, X. et al. A feedforward mechanism mediated by mechanosensitive ion channel PIEZO1 and tissue mechanics promotes glioma aggression. *Neuron* **100**, 799–815 (2018).

13. Zhang, J. & Reinhart-King, C. A. Targeting tissue stiffness in metastasis: mechanomedicine improves cancer therapy. *Cancer Cell* **37**, 754–755 (2020).
14. Mehlenbacher, R. D., Kolbl, R., Lay, A. & Dionne, J. A. Nanomaterials for in vivo imaging of mechanical forces and electrical fields. *Nat. Rev. Mater.* **3**, 17080 (2017).
15. Blanchard, A. T. & Salaita, K. Emerging uses of DNA mechanical devices. *Science* **365**, 1080–1081 (2019).
16. Brockman, J. M. et al. Live-cell super-resolved PAINT imaging of piconewton cellular traction forces. *Nat. Methods* **17**, 1018–1024 (2020).
17. Sun, W., Gao, X., Lei, H., Wang, W. & Cao, Y. Biophysical approaches for applying and measuring biological forces. *Adv. Sci.* **9**, 2105254 (2022).
18. Lee, C. et al. Giant nonlinear optical responses from photon-avalanching nanoparticles. *Nature* **589**, 230–235 (2021).
19. Boocock, D., Hino, N., Ruzickova, N., Hirashima, T. & Hannezo, E. Theory of mechanochemical patterning and optimal migration in cell monolayers. *Nat. Phys.* **17**, 267–274 (2021).
20. Miroshnikova, Y. A. et al. Adhesion forces and cortical tension couple cell proliferation and differentiation to drive epidermal stratification. *Nat. Cell Biol.* **20**, 69–80 (2018).
21. Petridou, N. I., Spiró, Z. & Heisenberg, C.-P. Multiscale force sensing in development. *Nat. Cell Biol.* **19**, 581–588 (2017).
22. Liu, C. et al. Heterogeneous microenvironmental stiffness regulates pro-metastatic functions of breast cancer cells. *Acta Biomater.* **131**, 326–340 (2021).
23. Midolo, L., Schliesser, A. & Fiore, A. Nano-opto-electro-mechanical systems. *Nat. Nanotechnol.* **13**, 11–18 (2018).
24. Tsoukalas, K., Lahijani, B. V. & Stobbe, S. Impact of transduction scaling laws on nanoelectromechanical systems. *Phys. Rev. Lett.* **124**, 223902 (2020).
25. Killeen, A., Bertrand, T. & Lee, C. F. Polar fluctuations lead to extensile nematic behavior in confluent tissues. *Phys. Rev. Lett.* **128**, 078001 (2022).
26. Wu, J., Lewis, A. H. & Grandl, J. Touch, tension, and transduction–the function and regulation of piezo ion channels. *Trends Biochem. Sci.* **42**, 57–71 (2017).
27. Liu, K., Liu, Y., Lin, D., Pei, A. & Cui, Y. Materials for lithium-ion battery safety. *Sci. Adv.* **4**, eaas9820 (2018).
28. Shan, X. et al. Sub-femtonewton force sensing in solution by super-resolved photonic force microscopy. *Nat. Photon.* **18**, 913–921 (2024).
29. Ichbiah, S., Delbary, F., McDougall, A., Dumollard, R. & Turlier, H. Embryo mechanics cartography: inference of 3D force atlases from fluorescence microscopy. *Nat. Methods* **20**, 1989–1999 (2023).
30. Bednarkiewicz, A., Chan, E. M., Kotulska, A., Marciniak, L. & Prorok, K. Photon avalanche in lanthanide doped nanoparticles for biomedical applications: super-resolution imaging. *Nanoscale Horiz.* **4**, 881–889 (2019).
31. Dudek, M. et al. Size-dependent photon avalanching in Tm^{3+} doped $LiYF_4$ nano, micro, and bulk crystals. *Adv. Opt. Mater.* **10**, 2201052 (2022).
32. Liang, Y. et al. Migrating photon avalanche in different emitters at the nanoscale enables 46th-order optical nonlinearity. *Nat. Nanotechnol.* **17**, 524–530 (2022).
33. Zhang, Z. et al. Tuning phonon energies in lanthanide-doped potassium lead halide nanocrystals for enhanced nonlinearity and upconversion. *Angew. Chem. Int. Ed.* **62**, e202212549 (2023).
34. Skripka, A. et al. A generalized approach to photon avalanche upconversion in luminescent nanocrystals. *Nano Lett.* **23**, 7100–7106 (2023).
35. Wu, S. et al. Non-blinking and photostable upconverted luminescence from single lanthanide-doped nanocrystals. *Proc. Natl Acad. Sci. USA* **106**, 10917–10921 (2009).
36. Park, Y. I. et al. Nonblinking and nonbleaching upconverting nanoparticles as an optical imaging nanoprobe and T1 magnetic resonance imaging contrast agent. *Adv. Mater.* **21**, 4467–4471 (2009).
37. Ostrowski, A. D. et al. Controlled synthesis and single-particle imaging of bright, sub-10 nm lanthanide-doped upconverting nanocrystals. *ACS Nano* **6**, 2686–2692 (2012).
38. Gargas, D. J. et al. Engineering bright sub-10-nm upconverting nanocrystals for single-molecule imaging. *Nat. Nanotechnol.* **9**, 300–305 (2014).
39. Lee, C. et al. Indefinite and bidirectional near-infrared nanocrystal photoswitching. *Nature* **618**, 951–958 (2023).
40. Cohen, B. E. Beyond fluorescence. *Nature* **467**, 407–408 (2010).
41. Tajon, C. A. et al. Photostable and efficient upconverting nanocrystal-based chemical sensors. *Opt. Mater.* **84**, 345–353 (2018).
42. Fischer, S., Bronstein, N. D., Swabeck, J. K., Chan, E. M. & Alivisatos, A. P. Precise tuning of surface quenching for luminescence enhancement in core–shell lanthanide-doped nanocrystals. *Nano Lett.* **16**, 7241–7247 (2016).
43. Johnson, N. J. et al. Direct evidence for coupled surface and concentration quenching dynamics in lanthanide-doped nanocrystals. *J. Am. Chem. Soc.* **139**, 3275–3282 (2017).
44. Szalkowski, M. et al. Predicting the impact of temperature dependent multi-phonon relaxation processes on the photon avalanche behavior in Tm^{3+}:$NaYF_4$ nanoparticles. *Opt. Mater. X* **12**, 100102 (2021).
45. Liu, X. et al. Extreme optical nonlinearity (>500) at room temperature through sublattice reconstruction. Preprint at *Research Square* https://doi.org/10.21203/rs.3.rs-4183918/v1 (2024).
46. Wisser, M. D. et al. Strain-induced modification of optical selection rules in lanthanide-based upconverting nanoparticles. *Nano Lett.* **15**, 1891–1897 (2015).
47. Lage, M. M., Moreira, R. L., Matinaga, F. M. & Gesland, J.-Y. Raman and infrared reflectivity determination of phonon modes and crystal structure of Czochralski-grown $NaLnF_4$ (Ln = La, Ce, Pr, Sm, Eu, and Gd) single crystals. *Chem. Mater.* **17**, 4523–4529 (2005).
48. van Swieten, T. P. et al. Extending the dynamic temperature range of Boltzmann thermometers. *Light Sci. Appl.* **11**, 343 (2022).
49. Casar, J. R., McLellan, C. A., Siefe, C. & Dionne, J. A. Lanthanide-based nanosensors: refining nanoparticle responsiveness for single particle imaging of stimuli. *ACS Photon.* **8**, 3–17 (2020).
50. McLellan, C. A. et al. Engineering bright and mechanosensitive alkaline-earth rare-earth upconverting nanoparticles. *J. Phys. Chem. Lett.* **13**, 1547–1553 (2022).
51. Kwock, K. W. et al. Surface-sensitive photon avalanche behavior revealed by single-avalanching-nanoparticle imaging. *J. Phys. Chem. C* **125**, 23976–23982 (2021).
52. Ribet, S. M. et al. Uncovering the three-dimensional structure of upconverting core–shell nanoparticles with multislice electron ptychography. *Appl. Phys. Lett.* **124**, 240601 (2024).
53. Majak, M., Misiak, M. & Bednarkiewicz, A. The mechanisms behind the extreme susceptibility of photon avalanche emission to quenching. *Mater. Horiz.* https://doi.org/10.1039/D4MH00362D (2024).
54. Runowski, M. et al. Lifetime nanomanometry—high-pressure luminescence of up-converting lanthanide nanocrystals—SrF_2:Yb^{3+},Er^{3+}. *Nanoscale* **9**, 16030–16037 (2017).
55. Dong, H., Sun, L.-D. & Yan, C.-H. Local structure engineering in lanthanide-doped nanocrystals for tunable upconversion emissions. *J. Am. Chem. Soc.* **143**, 20546–20561 (2021).
56. Sinatra, N. R. et al. Ultragentle manipulation of delicate structures using a soft robotic gripper. *Sci. Robot.* **4**, eaax5425 (2019).

Methods

Below we provide the detailed experimental methods used in this work. Much recent work has gone into development of diverse ANP compositions, consisting of different lanthanide species and various host materials[18,31–34,45,53,57,58]. In this study, we concentrated on one specific composition class—Tm^{3+}-doped $NaYF_4$ (ref. 18)—with the goal of showing how the photon-avalanche properties in general may be utilized for wide-dynamic-range force sensing of nanoscale environments. We anticipate that photon-avalanche-based force sensors will contribute to a diverse range of applications, spanning medicine[12,13,59] to biophysics[9,10,25,60–66], and robotics[8] to batteries[11,27,67,68]. With these specific ANP compositions, we detect previously remotely undetectable piconewton to micronewton forces—a complementary range to those of many other cutting-edge luminescent force-sensing methods that have been developed, which together cover forces from attonewtons to micronewtons[10,14–17,26,28,29,69–76].

Materials

Sodium trifluoroacetate (98%), gadolinium (III) chloride ($GdCl_3$, 99.9%+), thulium (III) chloride ($TmCl_3$, 99.9%+), yttrium (III) chloride (YCl_3, 99.9%+), ammonium fluoride (NH_4F, 99.9%), oleic acid (90%), octadecene (ODE, technical grade, 90%) and hexane (anhydrous, 99.5%) were purchased from Sigma-Aldrich. Sodium oleate (>97%) was purchased from TCI. All chemicals were used without any further purification.

Core synthesis

$NaYF_4$:Tm^{3+} core nanoparticles were synthesized using a previously described synthesis, with some modification[37]. $NaYF_4$:4% Tm^{3+} cores were synthesized as described further, and cores with other Tm^{3+} doping amounts were prepared analogously by varying the stoichiometric amounts of YCl_3 and $TmCl_3$. YCl_3 (0.96 mmol, 187.5 mg) and $TmCl_3$ (0.04 mmol, 11.0 mg) were added together with oleic acid (6 ml) and ODE (18 ml) to a dry 50-ml 3-neck round-bottom flask. The mixture was stirred, placed under a vacuum and heated to 100 °C for 1 h, causing the solution to become clear. The flask was then filled with nitrogen (N_2), and sodium oleate (2.5 mmol, 761.1 mg) and NH_4F (4 mmol, 148.1 mg) were added. The flask was subsequently placed under vacuum and the mixture was stirred for another 20 min, followed by N_2 flushing (×3). The reaction was heated to 320 °C and allowed to react under N_2. After 60 min of reaction time, the flask was rapidly cooled to room temperature by a strong stream of air, and nanoparticles were isolated using ethanol (20 ml) and centrifugation (3,000 rpm, 5 min). The nanoparticles were additionally washed with hexane:ethanol (1:1 v/v) twice and redispersed in 4 ml of hexane for storage.

Preparation of shell precursors

Epitaxial $NaYF_4$:20% Gd^{3+} shells were grown on the doped $NaYF_4$:Tm^{3+} cores in a N_2-filled glovebox with laboratory automation robot Workstation for Automated Nanocrystal Discovery and Analysis (WANDA)[77]. Precursor solution, corresponding to the composition of the epitaxially grown shell layer, was prepared by heating stoichiometric amounts of lanthanide chlorides ($LnCl_3$, 2.5 mmol of total amount) to 110 °C in oleic acid (10 ml) and ODE (15 ml), and stirring for 15 min under vacuum. The flask was filled with N_2 and heated to 160 °C for 30 min to allow the $LnCl_3$ to dissolve, which was followed by another 15 min at 110 °C under vacuum, rendering a 0.1 M solution of stoichiometric mixture of lanthanide oleates. In a separate flask, a Na and F precursor was prepared by dissolving sodium trifluoroacetate (8 mmol, 1,088 mg) in oleic acid (20 ml) and ODE (20 ml) and applying vacuum at room temperature for 60 min, resulting in a 0.2 M sodium trifluoroacetate oleate solution.

Synthesis of core/shell $NaYF_4$:Tm^{3+}/$NaYF_4$:20% Gd^{3+} nanoparticles

$NaYF_4$:20% Gd^{3+} shells of 5–9 nm thickness were grown on the core nanoparticles using a layer-by-layer protocol similar to that used in ref. 78. In brief, for a shell thickness of 6 nm, 6 ml ODE and 4 ml oleic acid were added to the dried cores and heated to 280 °C at 20 °C min^{-1} in the WANDA glovebox. The automated protocol alternated between injections of a 0.2 M sodium trifluoroacetate oleate stock solution and a 0.1 M stock solution of 20% gadolinium and 80% yttrium oleate. One injection was performed every 20 min for a total of 32 injections (16 injections for each precursor). Following the last injection, each reaction was annealed at 280 °C for an additional 30 min and then cooled rapidly by N_2 flow. The particles were isolated and purified according to the purification protocol described for the cores.

Structural characterization

Transmission electron microscopy images were obtained by a transmission electron microscope (JEOL 2100 F) with an accelerating voltage of 200 kV. Powder X-ray diffraction patterns were acquired with a Bruker AXS D8 Discover GADDS X-ray diffractometer, using Co Kα radiation. The Tm^{3+} doping concentration in the cores was measured by elemental analysis using inductively coupled plasma optical emission spectroscopy (measurements performed by Galbraith Laboratories).

Single-particle sample preparation

A volume of approximately 40 µl of 0.02–0.1 nM particle suspension in hexane was spin-coated at 1–3 krpm for 1 min on sterilized poly-L-lysine-coated 170-µm-thick glass coverslips (Electron Microscopy Sciences 72292-20). Prepared single-particles-on-glass samples were stored at ambient conditions before AFM and optical measurements. The single-particle dispersity (about 2 µm between particles) of the sample was verified by AFM scanning and optical scanning of the sample.

Mechano-optical set-up

All measurements were carried out with a custom-designed combined AFM atop an inverted optical microscope, based on a Horiba Trios system, operating in ambient conditions. Modifications were made to accommodate usage of thin, transparent samples and high-numerical-aperture oil immersive objectives without experiencing mechanical vibrations. Elimination of acoustic noise included the design of screw-in, small (diameter of about 4 mm) aperture, sample holders and an acoustic-foam-lined isolation chamber. Reduction of structural vibrations was attained by high-mass support for the microscope base, a heavy base for the microscope objective and Sorbothane isolation of the microscope breadboard.

Mechano-optical measurements

After location of a single particle and verification of a single, rather than clustered, entity by ensuring its brightness was lower than the cut-off maximal brightness expected for a single particle at the corresponding excitation intensity or by AFM scanning at high resolution, its power-dependent emission was characterized at ambient conditions. For power-dependent measurements, a gradient neutral-density wheel was rotated by a computer-driven program; excitation powers were measured by diverting about 10% of the excitation power exiting the neutral-density wheel to a power meter by a thin glass slide placed at an angle to the excitation-path axis. Excitation intensities were calculated using measured excitation powers and dividing by the area calculated from the image of the focused laser spot. Excitation of the sample and collection of its emission were both through a ×60, 1.4-numerical-aperture, oil objective (Nikon CFI Plan Apochromat Lambda) located beneath the sample. Excitation of the particles was carried out with a continuous-wave 1,064-nm laser diode (QPhotonics), after filtering with 900-nm long-pass and 950-nm long-pass filters. Emission from the particles was filtered with 850-nm short-pass, 945-nm short-pass and 950-nm short-pass filters, before it was measured by the LabRAM spectrometer FIVS Synapse EM-CCD camera (EM-CCD; electron multiplying charge coupled device). A full spectrum was recorded by a row of 1,600 active pixels within the CCD array. Integrated intensities were calculated by performing Riemann

sums over the desired spectral ranges (while each pixel corresponded to about 0.125 nm), subtracting the root mean square of the dark counts (integrated intensities of the background level), dividing by the electron-multiplier gain (adjustable photon-to-count number multiplication factor; electron-multiplier gain ≤10), and correcting for the wavelength-specific quantum efficiency (QE(λ) ≤ 0.5) of the camera. Silicon AFM force-modulation probes with spring constants of 0.8–8.9 N m^{-1} and resonance frequencies of 36–98 kHz (ACCESS-FM Probes, Applied Nanostructures) were utilized for tapping mode scanning and for force application. Cantilever resonance frequencies were measured and spring constants were determined via the Sader method. Force versus tip–sample distance sweeps were performed for force calibration of the probes. The tip radius of curvature according to the specifications was 6 nm; application of 2.5-μN force (the maximum force applied in this study) increased tip bluntness and radius of curvature, as the force magnitude was larger than silicon's plastic deformation threshold (Supplementary Note 8). Application of force on a particle was gradual (force increments ≤125 nN), to prevent particle displacement. Optical scanning of the particle before and after compression cycles was carried out to ensure no sample drift or particle displacement occurred owing to force application; inconsistency between these scans rendered the data acquired in between discardable. Decompression cycles were not analysed for this study, as all the measurements were carried out at ambient conditions, where the adhesion force arising from the condensed meniscus upon the tip and particle[79,80] opposes tip retraction.

Data analysis

Single-particle spectra were fit to a sum of two to six Gaussians, as appropriate, for each Tm^{3+} transition. Emissions at 800 nm and 700 nm were integrated from 760–840 nm and 675–720 nm, respectively, with CCD electron-multiplier gain and QE(λ) corrections. Each particle was compressed several times at each excitation intensity. For both the pre-ANPs and ANPs, each compression cycle of 800 nm emission (P) versus force (F) dataset was fitted to a linear polynomial of the form $P = aF + b$, where $b = I_0t$ and $a = I_0tR$. The particle response R, as well as the force resolution $\left(\frac{1}{|R|\sqrt{I_0t}}\right)$, were derived from the fit a and b values. The accessible force range was derived from the fit F value at $P = 0$ for the ANPs; the force range for the pre-ANPs was that yielding the fit with the maximal positive slope. For the piezochromic ANPs, each compression cycle 800 nm/700 nm emission ratio (α) versus force (F) dataset was fitted to a linear polynomial of the form $\alpha = aF + b$, where $b = \alpha_0$ and $a = \alpha_0R$. The particle response R, as well as the force resolution $\left(\frac{1+\alpha_0}{|R|\sqrt{I_0t\alpha_0}}\right)$, were derived from the fit a and b values. The accessible force range was determined by the 700-nm emission signal-to-noise ratio, such that the signal-to-noise ratio was about 1. NES values were derived from multiplication of the measured noise-derived forces by the square roots of measurement integration times (Supplementary Note 7). Standard errors on each of the values were propagated from the standard errors on the fit values, which were derived from Δa and Δb, which are 95% confidence intervals of the fitted values.

Data availability

All data generated or analysed during this study, which support the plots within this paper and other findings of this study, are included in this published article and its Supplementary Information. Source data are provided with this paper.

Code availability

The code for modelling the force-dependent photon avalanche using the differential rate equations described in Supplementary Information is freely available on Zenodo at https://doi.org/10.5281/zenodo.13380752 (ref. 81).

57. Skripka, A. et al. Intrinsic optical bistability of photon avalanching nanocrystals. *Nat. Photon.* https://doi.org/10.1038/s41566-024-01577-x (2025).
58. Wang, C. et al. Tandem photon avalanches for various nanoscale emitters with optical nonlinearity up to 41st-order through interfacial energy transfer. *Adv. Mater.* **36**, 2307848 (2024).
59. Kaushik, S. & Persson, A. I. Unlocking the dangers of a stiffening brain. *Neuron* **100**, 763–765 (2018).
60. Romani, P., Valcarcel-Jimenez, L., Frezza, C. & Dupont, S. Crosstalk between mechanotransduction and metabolism. *Nat. Rev. Mol. Cell Biol.* **22**, 22–38 (2021).
61. Jain, S. et al. The role of single-cell mechanical behaviour and polarity in driving collective cell migration. *Nat. Phys.* **16**, 802–809 (2020).
62. De Belly, H., Paluch, E. K. & Chalut, K. J. Interplay between mechanics and signalling in regulating cell fate. *Nat. Rev. Mol. Cell Biol.* **23**, 465–480 (2022).
63. Qiu, Y., Myers, D. R. & Lam, W. A. The biophysics and mechanics of blood from a materials perspective. *Nat. Rev. Mater.* **4**, 294–311 (2019).
64. Van Helvert, S., Storm, C. & Friedl, P. Mechanoreciprocity in cell migration. *Nat. Cell Biol.* **20**, 8–20 (2018).
65. Firmin, J. et al. Mechanics of human embryo compaction. *Nature* **629**, 646–651 (2024).
66. Yeoman, B. et al. Adhesion strength and contractility enable metastatic cells to become adurotactic. *Cell Rep.* **34**, 108816 (2021).
67. Huang, W. et al. Onboard early detection and mitigation of lithium plating in fast-charging batteries. *Nat. Commun.* **13**, 7091 (2022).
68. Doux, J. M. et al. Stack pressure considerations for room-temperature all-solid-state lithium metal batteries. *Adv. Energy Mater.* **10**, 1903253 (2020).
69. Brockman, J. M. et al. Mapping the 3D orientation of piconewton integrin traction forces. *Nat. Methods* **15**, 115–118 (2018).
70. Serwane, F. et al. In vivo quantification of spatially varying mechanical properties in developing tissues. *Nat. Methods* **14**, 181–186 (2017).
71. Stabley, D. R., Jurchenko, C., Marshall, S. S. & Salaita, K. S. Visualizing mechanical tension across membrane receptors with a fluorescent sensor. *Nat. Methods* **9**, 64–67 (2012).
72. Nickels, P. C. et al. Molecular force spectroscopy with a DNA origami-based nanoscopic force clamp. *Science* **354**, 305–307 (2016).
73. Ringer, P. et al. Multiplexing molecular tension sensors reveals piconewton force gradient across talin-1. *Nat. Methods* **14**, 1090–1096 (2017).
74. Campàs, O. et al. Quantifying cell-generated mechanical forces within living embryonic tissues. *Nat. Methods* **11**, 183–189 (2014).
75. Polacheck, W. J. & Chen, C. S. Measuring cell-generated forces: a guide to the available tools. *Nat. Methods* **13**, 415–423 (2016).
76. Vian, A. et al. In situ quantification of osmotic pressure within living embryonic tissues. *Nat. Commun.* **14**, 7023 (2023).
77. Chan, E. M. et al. Reproducible, high-throughput synthesis of colloidal nanocrystals for optimization in multidimensional parameter space. *Nano Lett.* **10**, 1874–1885 (2010).
78. Levy, E. S. et al. Energy-looping nanoparticles: harnessing excited-state absorption for deep-tissue imaging. *ACS Nano* **10**, 8423–8433 (2016).
79. Wallace, A. *Scanning Probe Microscopy. Analytical Geomicrobiology: A Handbook of Instrumental Techniques* 121–147 (Cambridge Univ. Press, 2019).
80. Xiao, C. et al. Thickness and structure of adsorbed water layer and effects on adhesion and friction at nanoasperity contact. *Colloids Interfaces* **3**, 55 (2019).
81. Fardian-Melamed, N. et al. Infrared nanosensors of pico- to micro-newton forces. *Zenodo* https://doi.org/10.5281/zenodo.13380752 (2024).

Acknowledgements We thank K. W. C. Kwock and R. G. Stark for assistance with the set-up configuration. N.F.-M. acknowledges support from the European Union's Horizon 2020 research and innovation programme under the Marie Skłodowska-Curie grant agreement number 893439, the US Department of State – IL Fulbright Scholarship Program, the Zuckerman–CHE STEM Leadership Program, the Israel Scholarship Education Foundation (ISEF), the ISEF – de Gunzburg International Science Fellowship Program, and the Weizmann Institute's Women's Postdoctoral Career Development Award. B.U. and P.J.S. acknowledge support by the National Science Foundation under grant number CHE-2203510. A.S. acknowledges the support from the European Union's Horizon 2020 research and innovation programme under the Marie Skłodowska-Curie grant agreement number 895809 (MONOCLE). Work at the Molecular Foundry was supported by the Office of Science, Office of Basic Energy Sciences, of the US Department of Energy under contract number DE-AC02-05CH11231. X.Q., B.E.C. and E.M.C. were supported in part by the Defense Advanced Research Projects Agency (DARPA) ENVision programme under contract HR0011257070, and C.L. and P.J.S. under DARPA ENVision contract HR00112220006. T.P.D. and P.J.S. also acknowledge support for scan-probe instrumentation and measurement capabilities from Programmable Quantum Materials, an Energy Frontier Research Center funded by the US DOE, Office of Science, Basic Energy Sciences (BES), under award DE-SC0019443.

Author contributions Conceptualization: N.F.-M. and P.J.S. Experimental design: N.F.-M. and P.J.S. Experimental set-up: N.F.-M., B.U., T.P.D. and C.L. Mechano-optical measurements: N.F.-M., M.W., J.M.G. and P.J.S. Mechano-optical data analysis: N.F.-M., B.U. and C.L. Theoretical modelling and simulations: N.F.-M., E.M.C., A.S., C.L., P.J.S. and B.U. Advanced nanocrystal synthesis and structural characterization: A.S., A.T., X.Q., B.E.C. and E.M.C. Single-nanocrystal sample preparation: N.F.-M. and C.L. Paper writing: all authors.

Competing interests The authors declare no competing interests.

Additional information

Supplementary information The online version contains supplementary material available at https://doi.org/10.1038/s41586-024-08221-2.

Correspondence and requests for materials should be addressed to Natalie Fardian-Melamed, Bruce E. Cohen, Emory M. Chan or P. James Schuck.

Peer review information *Nature* thanks Andries Meijerink, Jon R. Pratt and the other, anonymous, reviewer(s) for their contribution to the peer review of this work. Peer reviewer reports are available.

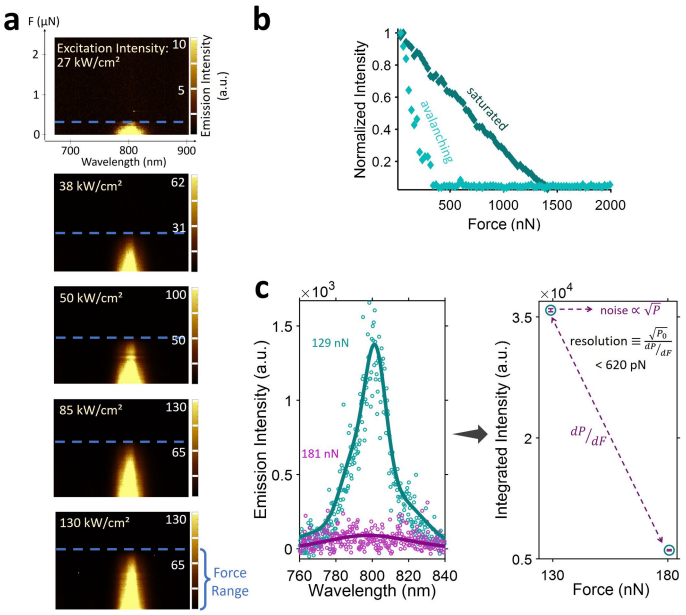

Extended Data Fig. 1 | Avalanche-shifting (7% Tm^{3+}) ANP mechano-optics at the avalanching and saturation regimes. a. Emission spectra as a function of applied force, for increasing excitation intensities, for single ANPs. At each excitation intensity, 100 force-dependent optical spectra are measured per 2.5 μN force ramp. The accessible force range (dashed line), and the relative brightness of the ANP (note different scales) for each excitation intensity correlate with avalanching behavior. **b**. Full compression cycles, each consisting of 100 emission intensity versus applied force data points, for single ANPs excited in their avalanching regime (27 kW cm^{-2}) and saturation regime (85 kW cm^{-2}). Each data point is derived from a single force-dependent optical spectrum (as in **a** and **c**). **c**. Two sequentially measured emission spectra (left) and their corresponding integrated intensities (right) as a function of applied force, for an ANP excited in its avalanching regime (18 kW cm^{-2}). Error bars for integrated emission intensities are based on signal Poissonian statistics. The noise-defined resolution, retrieved from a full compression cycle (as in **a** and **b**), is depicted (P is photon counts (integrated intensity), F is force, P_0 is the photon count at F = 0). Integration time is 3 s for all measurements.

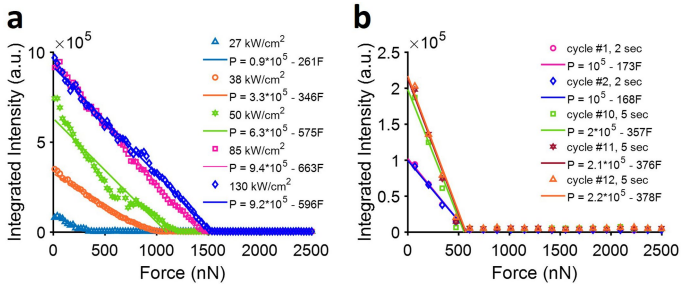

Extended Data Fig. 2 | Mechano-optical response of single avalanche-shifting (7% Tm^{3+}) ANPs. a. Excitation power dependence of the mechano-optical response of a single ANP. Each compression cycle (measured at a different excitation intensity) consists of 100 data points, derived from 100 force-dependent optical spectra measured at 3 s acquisition times. Force increment step size is 25nN. Excitation intensities and fitted graph equations (where P is emission intensity and F is force) for each compression cycle are depicted within the legend. **b**. Mechano-optical response cyclability of a single ANP. Repeating compression cycles measured for a single ANP at a specific excitation power (27 kW cm^{-2}), for different acquisition times. Each compression cycle consists of 20 data points, derived from 20 force-dependent optical spectra measured at 2 s (cycles 1, 2) and 5 s (cycles 10, 11, 12) acquisition times. The force-dependent optical response is repeatable, for the 2.5-μN-force cycles applied. No photodegradation or plastic deformation is measured under these excitation and mechanical conditions, for up to 25 measured cycles per particle. The difference in apparent ambient particle brightness, and hence emission-force graphs, derives from the different acquisition times (noted for each cycle in the figure legend). Normalization by the acquisition time yields similar noise-equivalent sensitivity (NES) values for all cycles.

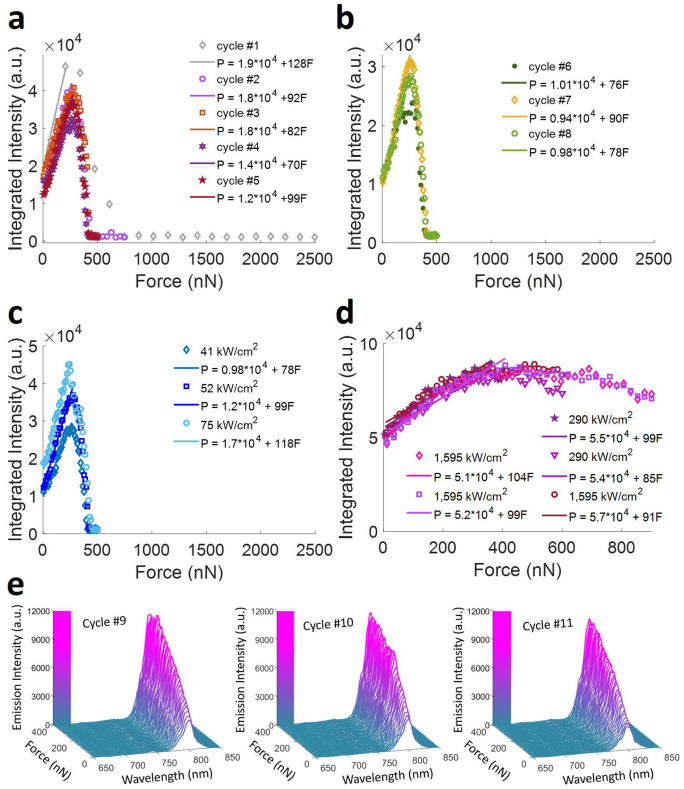

Extended Data Fig. 3 | Cyclability of single (4% Tm^{3+}) pre-ANP to ANP transitions. a-b. Recurring compression cycles on a single pre-ANP excited at 52 kW cm^{-2} (**a**) and 41 kW cm^{-2} (**b**). For each cycle, once the particle reaches its maximal emission (at the same force value, within the measurement error), its emission decreases with force following an ANP response to force. Cycle number and fitted graph equations (where P is emission intensity and F is force) for each compression cycle are depicted within the legend. **c-d**. Excitation power dependent compression cycles for single pre-ANPs at the low-power regime (**c**) and at the high-power regime (**d**). Excitation intensities and fitted graph equations (where P is emission intensity and F is force) for each compression cycle are depicted within the legend. For each cycle, once the particle reaches its maximal emission (at the same force value, within the measurement error), its emission decreases with force following an ANP response to force. **e**. Emission increase force range of compression cycles #9, #10, and #11, of a pre-ANP measured at ~1,800 kW cm^{-2}. **a-e**. Integration time per unit force was 3 s for all compression cycles.

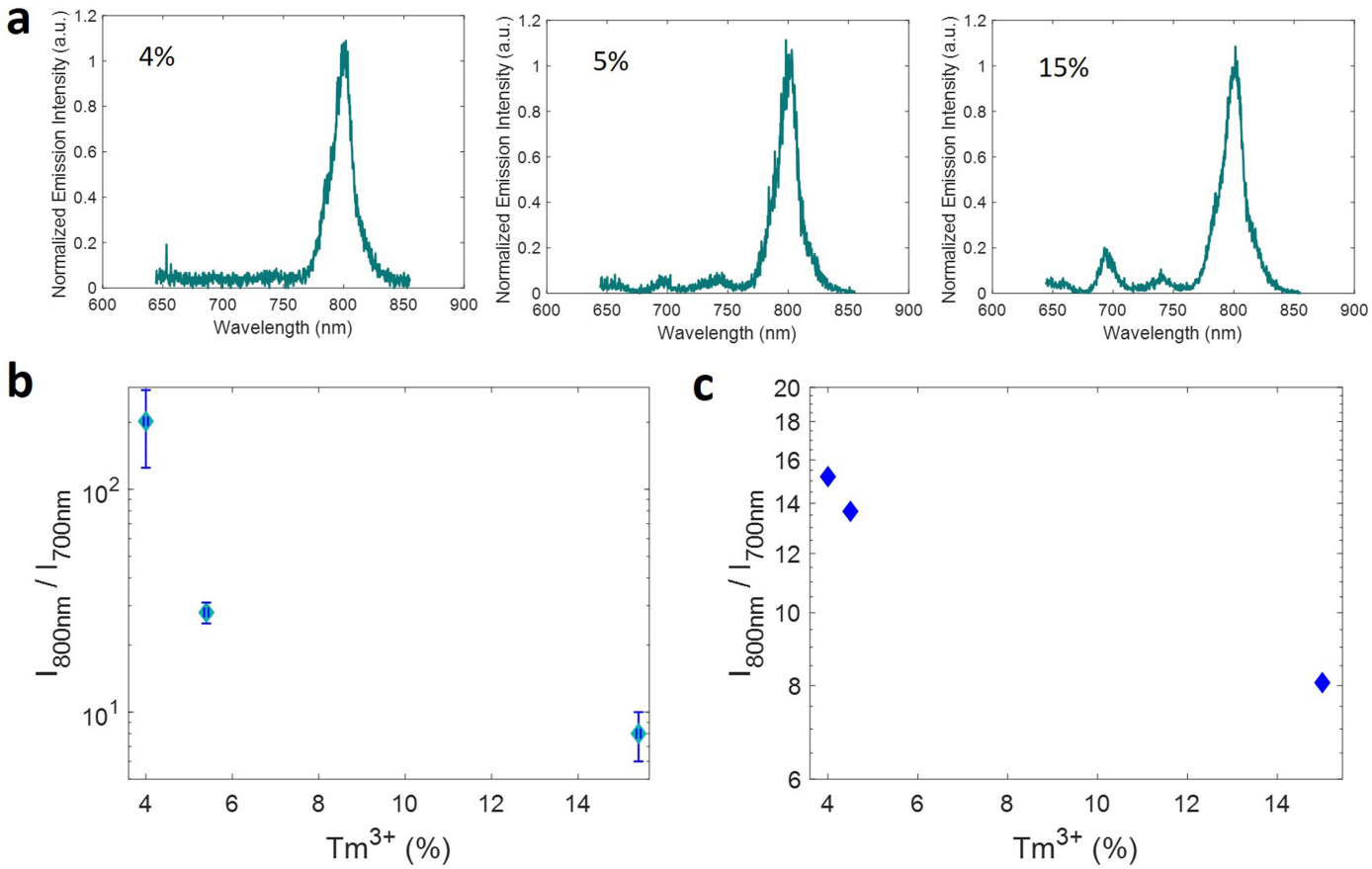

Extended Data Fig. 4 | Measurements and simulations of the 800 nm/ 700 nm -emission as a function of Tm^{3+} concentration. a. Single particle spectra, measured for different Tm^{3+} concentration pre-ANPs/ANPs, at their respective saturation regimes (excitation wavelength: 1064 nm; excitation intensity: 376 kW cm^{-2} (4% Tm^{3+}), 1,849 kW cm^{-2} (5% Tm^{3+}), 517 kW cm^{-2} (15% Tm^{3+})). **b**. 800 nm / 700 nm -emission ratio as a function of Tm^{3+} concentration for different Tm^{3+} concentration pre-ANPs/ANPs, measured at their respective saturation regimes (excitation wavelength: 1064 nm; excitation intensity: 376 kW cm^{-2} (4% Tm^{3+}), 1,849 kW cm^{-2} (5% Tm^{3+}), 517 kW cm^{-2} (15% Tm^{3+})). Error bars are the standard deviations of three single-NP measurements. **c**. Photon avalanche differential rate equation (DRE) model simulations of the 800 nm / 700 nm -emission ratio as a function of Tm^{3+} concentration. The DRE simulations for the different Tm^{3+} concentrations were performed with the respective parameters (per Tm^{3+} concentration) extracted from fitting the emission versus excitation graphs measured at zero applied force (Supplementary Note 6, Table S3, and Fig. S5). Note that the DRE model predicts Tm^{3+} emissions from these levels up to a certain excitation threshold, above which other, higher-level, excited states are populated and thus must be taken into account. Any discrepancies between the simulated values here and the measured ones in **a**-**b** may be accounted for by adding DREs for higher levels (above $^3F_2$). Other factors – such as determination of exact concentrations and hence energy transfer rates, or discernment of the precise 700 nm emission at lower concentrations and hence experimental 800 nm / 700 nm -emission ratios – may also reduce discrepancies between simulated and measured values. The DRE simulations show that higher cross-relaxation rates, attained at higher Tm^{3+} concentrations, decrease the 800 nm / 700 nm -emission ratio by: **1**. Populating $^3F_4$ at a faster rate, which, in turn, populates $^3F_3$ at a faster rate by direct excited state absorption. **2**. Depopulating $^3H_4$ at a faster rate.

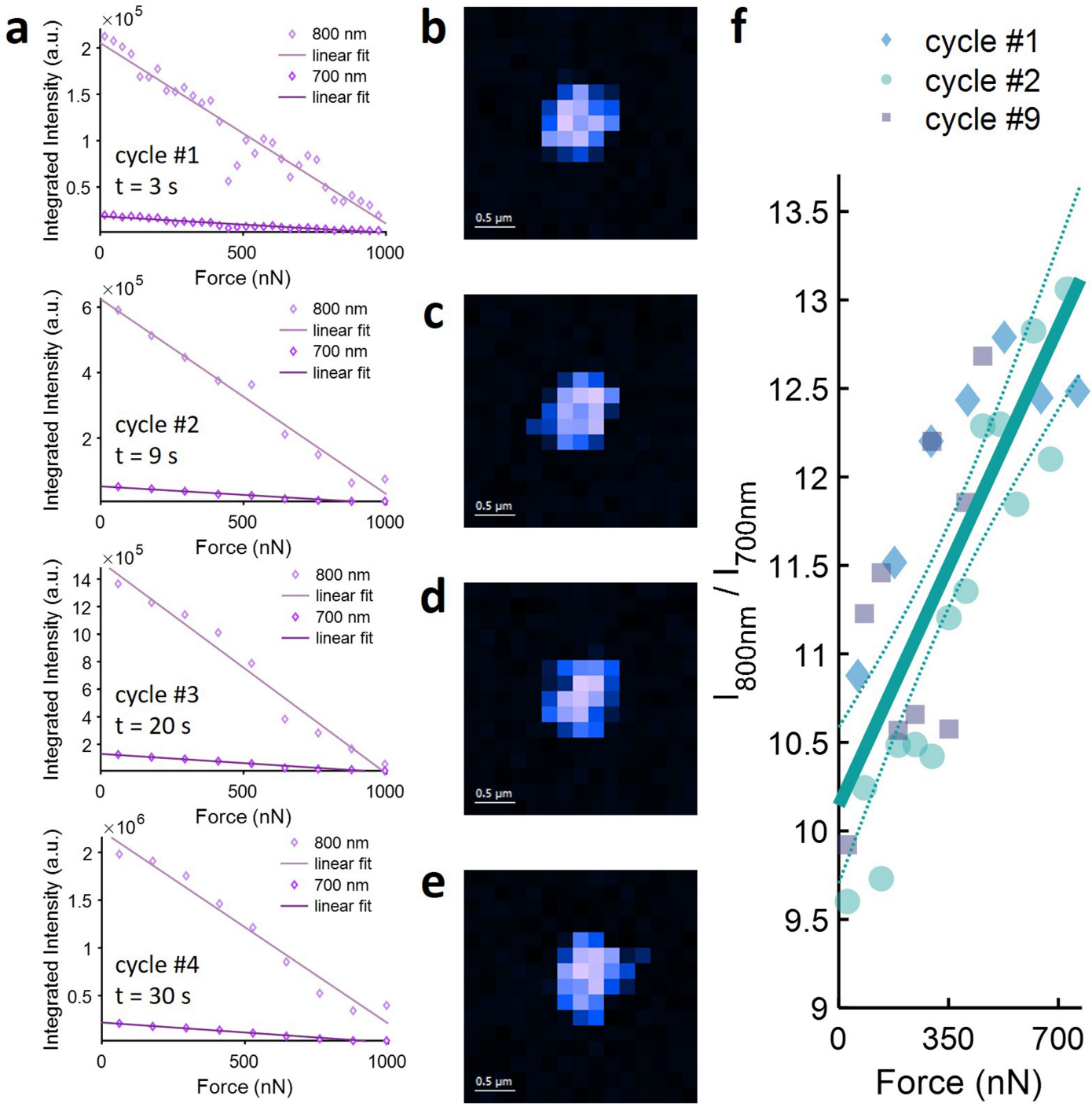

Extended Data Fig. 5 | Mechano-optical response cyclability of single (15% Tm^{3+}) piezochromic ANPs. a. 800 nm and 700 nm integrated emission intensity versus applied force, for 4 consecutive force cycles, attained for a single piezochromic ANP. A total of up to 1.5 µN force was applied on the particle at each compression cycle. Each full compression cycle consists of 10–50 force-spectrum data points. Integration time per data point was: 3 s (cycle #1), 9 s (cycle #2), 20 s (cycle #3), and 30 s (cycle #4). **b**-**e**. Hyperspectral imaging of a single piezochromic ANP, before compression cycle #1 (**b**), #2 (**c**), and #9 (**d**), and after cycle #9 (**e**). Corresponding compression cycles displayed in **f**. Sampling time: 0.3 s. **f**. 800 nm / 700 nm -emission ratio versus applied force, for three force cycles, attained for a single piezochromic ANP (pre- and post-imaging in **a**-**d**). A total of 1 µN force was applied on the particle at each compression cycle. Each full compression cycle consists of 10–20 force-spectrum data points. Integration time per data point was: 30 s (cycle #1), 50 s (cycle #2), and 3 s (cycle #9). **a**-**f**. Excitation intensity: 1,131 ± 46 kW cm^{-2}.

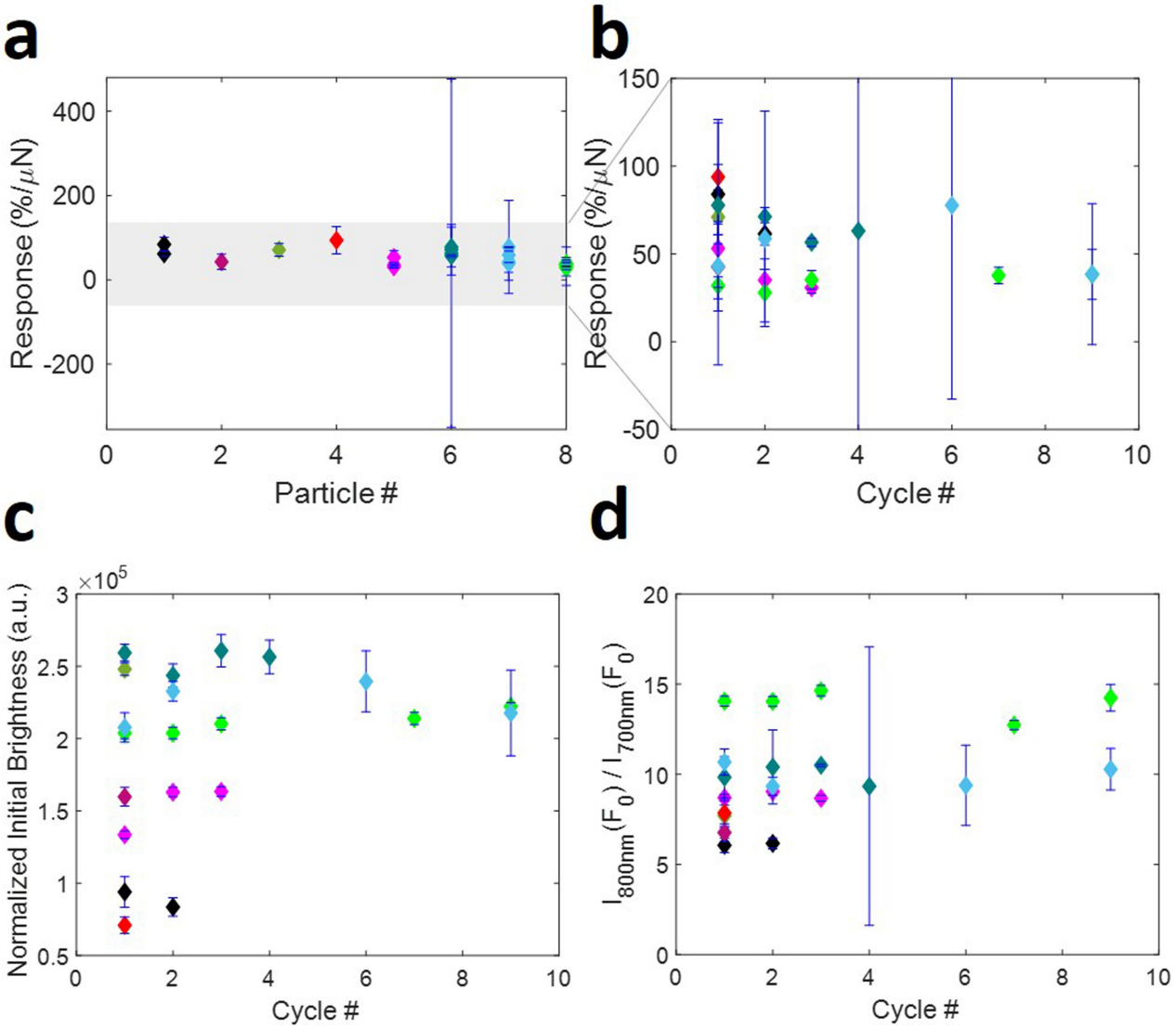

Extended Data Fig. 6 | Mechano-optical response versus cycle # for single (15% Tm^{3+}) piezochromic ANPs. a. Mechano-optical response (percent change of the 800 nm / 700 nm -emission ratio versus applied force), for up to 9 compression cycles per particle, for 8 different piezochromic ANPs. **b**-**d**. Mechano-optical response (**b**), normalized initial (F = 0) brightness (**c**), and initial (F = 0) 800 nm / 700 nm -emission ratio (**d**) versus cycle #. Data are derived from 21 compression cycles on 8 piezochromic ANPs (excitation intensity: 1,131 ± 46 kW cm^{-2}). Each compression cycle consists of 10–1000 emission versus force data points. Error bars depict the extrapolated errors derived from the 800 nm / 700 nm -emission ratio versus applied force fit values' 95% confidence intervals, while compression cycles consisting of a lower number of emission-versus-force data points yield larger S.E.M.s. Data points in **c** are normalized to a 3 s integration time baseline (i.e., divided by their respective integration times, and multiplied by 3 s), so as to conform to data acquired for the other (pre-avalanching and avalanching) particles in this study – for comparison between particles (data in **c** was further normalized to a 1 s integration time baseline for NES derivation). Data in **b**, **c**, and **d** are colour-coded as in **a** (each colour represents a different single particle).

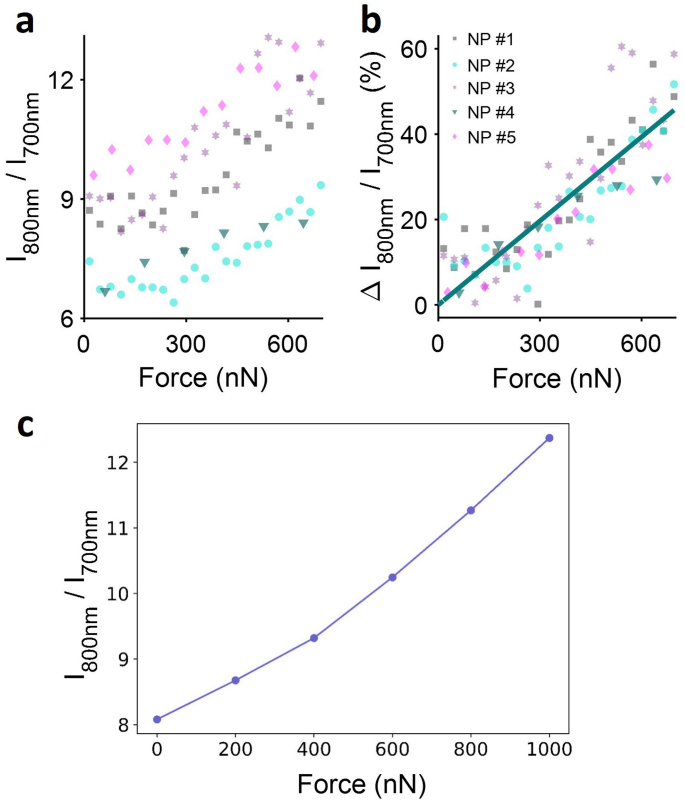

Extended Data Fig. 7 | Measurements and simulations of the mechano-optical response of single (15% Tm^{3+}) piezochromic ANPs. Measured 800 nm / 700 nm -emission ratio (**a**) and percent change of the 800 nm / 700 nm -emission ratio (**b**) versus applied force, for 5 compression cycles originating from 5 different piezochromic ANPs (excitation intensity: 1,131 ± 46 kW cm^{-2}). Integration time per data point was: 3 s (NP #1), 3 s (NP #2), 3 s (NP #3), 30 s (NP #4), and 50 s (NP #5). While their initial 800 nm / 700 nm -emission ratios differ by up to ±25% (full statistics in Extended Data Fig. 8), their mechanical response is similar. **c**. Photon avalanche DRE model simulations of the 15% Tm^{3+} piezochromic ANP force response. All DRE parameters are listed in Supplementary Note 6, Table S3. Zero-force simulation parameters are derived from fitting the excitation (at 1064 nm) versus emission (at 800 nm) data measured for piezochromic ANPs at ambient conditions (Supplementary Note 6, Fig. S5c). Force dependence of all of the nonradiative relaxation and cross-relaxation rates are derived from the equations listed in Supplementary Note 6. Calculations were performed for excitation intensities ca. 20-fold higher than threshold intensities, in line with the excitation power densities used for the piezochromic ANP measurements in this study.

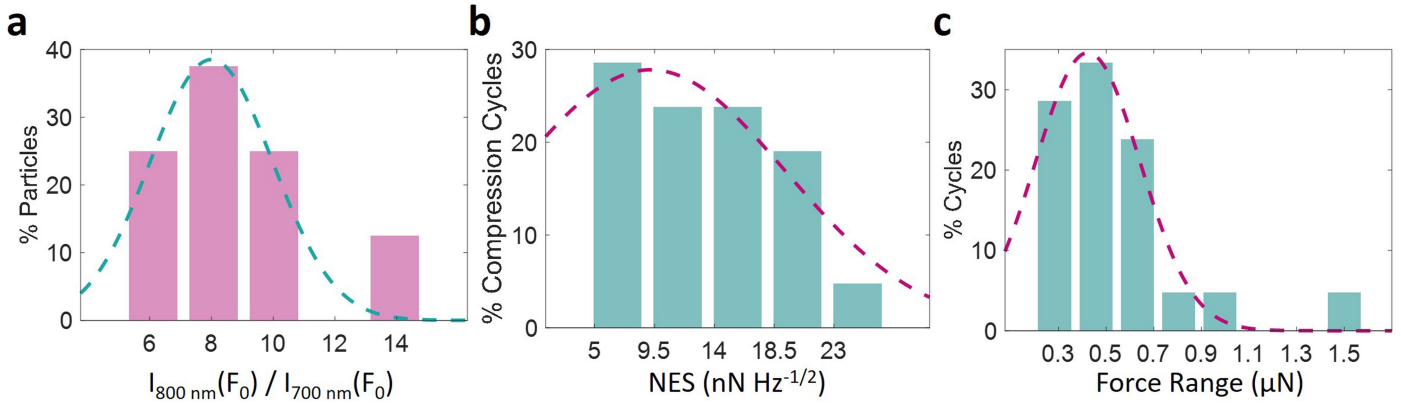

Extended Data Fig. 8 | Mechano-optical parameter distributions for single (15% Tm^{3+}) piezochromic ANPs. Initial (F = 0) 800 nm / 700 nm -emission ratio (**a**), noise-equivalent sensitivity (NES) (**b**), and force range (**c**) population distributions, along with their histogram Gaussian fits, for 21 compression cycles measured for 8 piezochromic ANPs (excitation intensity: 1,131 ± 46 kW cm^{-2}). Each compression cycle consists of 10–1000 emission versus force data points, measured at different integration times (3–50 s). The normal distribution fits yield means and S.E.M.s of: $I_{800\,nm}(F_0) / I_{700\,nm}(F_0)$ = 8.0 ± 0.7 (**a**), NES = 9.2 ± 2.0 nN $Hz^{-1/2}$ (**b**), and F_{range} = 0.4 ± 0.04 μN (**c**).

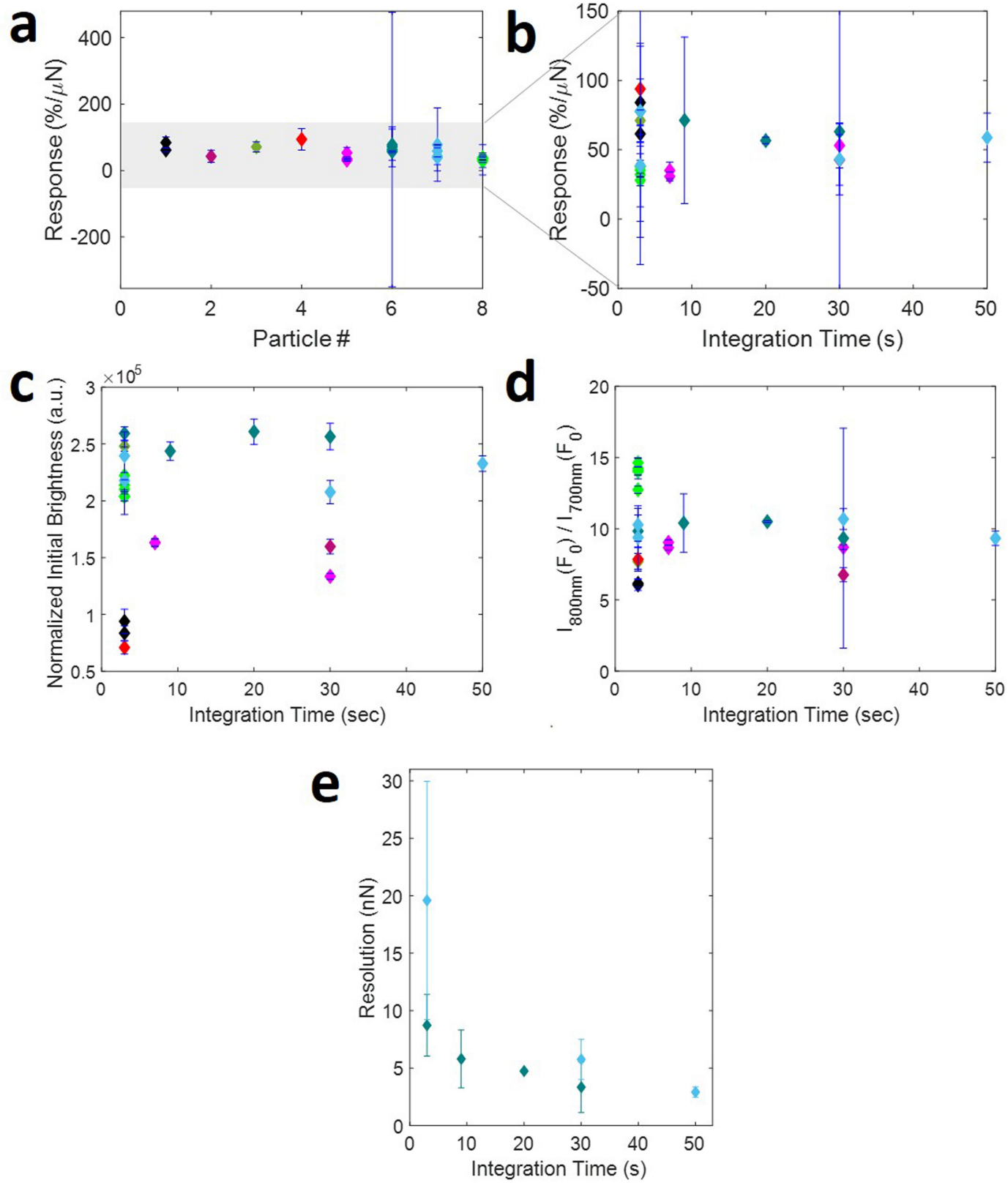

Extended Data Fig. 9 | See next page for caption.

Extended Data Fig. 9 | Mechano-optical response and resolution as a function of integration time for single (15% Tm^{3+}) piezochromic ANPs. **a**. Mechano-optical response (percent change of the 800 nm / 700 nm -emission ratio versus applied force), for up to 9 compression cycles per particle, for 8 different piezochromic ANPs. **b**-**d**. Mechano-optical response (**b**), normalized initial (F = 0) brightness (**c**), and initial (F = 0) 800 nm / 700 nm -emission ratio (**d**) versus integration time. Data are derived from 21 compression cycles on 8 piezochromic ANPs. Data points in **c** are normalized to a 3 s integration time baseline (see Extended Data Fig. 6). Data in **b**, **c**, and **d** are colour-coded as in **a** (each colour represents a different single particle). **e**. Resolution of (15% Tm^{3+}) piezochromic ANPs as a function of integration time. Resolutions are derived from 7 compression cycles on two 15% Tm^{3+} piezochromic ANPs with different initial (F = 0) brightnesses. **a**-**e**. Excitation intensity: 1,131 ± 46 kW cm^{-2}. Each compression cycle consists of 10–1000 emission versus force data points. Error bars depict the extrapolated errors derived from the 800 nm / 700 nm -emission ratio versus applied force fit values' 95% confidence intervals, while compression cycles consisting of a lower number of emission-versus-force data points yield larger S.E.M.s.

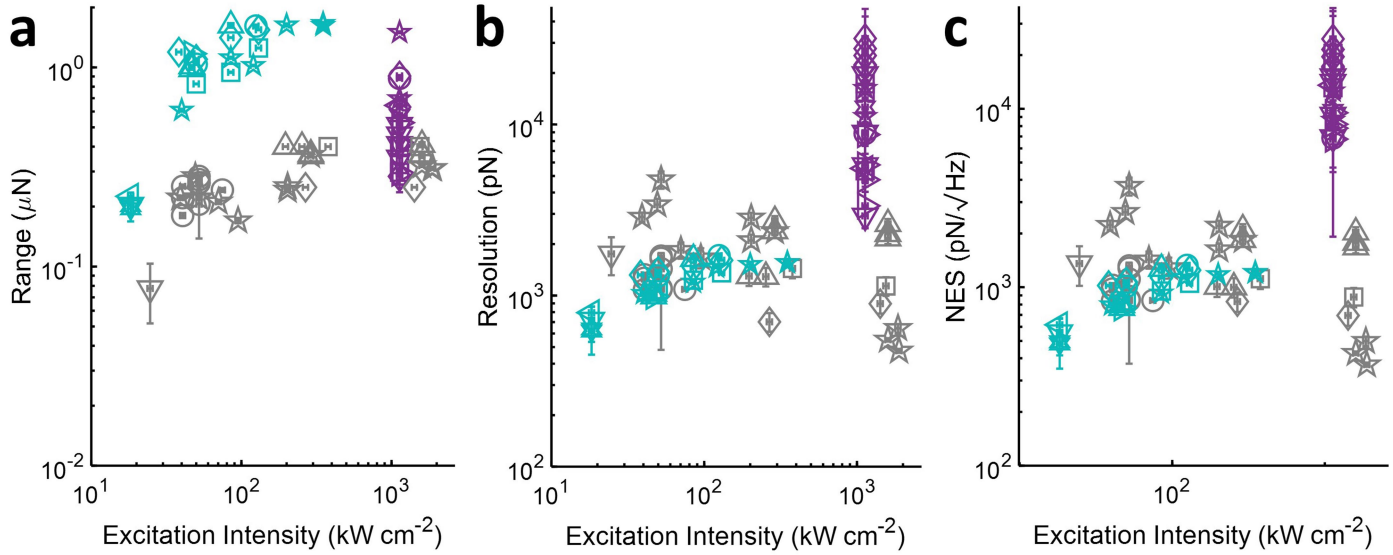

d

Sensing Modality	Tm^{3+} Doping Concentration	NP Average Diameter (nm)	Core/Shell Size (nm)	Excitation Intensity ($kW\ cm^{-2}$)	NES (*N* = 3 NPs)
Avalanche-Shifting	7%	33	16 / 8.5	18 ± 1	554 ± 52 $pN/\sqrt{Hz}$
Mechanobrightening	4%	44	32 / 6	35 ± 7	1.5 ± 0.5 $nN/\sqrt{Hz}$
Mechanochromism	15%	39	21 / 9	1131 ± 45	8.2 ± 1.2 $nN/\sqrt{Hz}$

Extended Data Fig. 10 | ANP (7% Tm^{3+}) avalanche-shifting, pre-ANP (4% Tm^{3+}) mechanobrightening, and piezochromic ANP (15% Tm^{3+}) mechanochromism parameters versus excitation intensity. Force range (**a**), force resolution (**b**), and noise-equivalent sensitivity (NES) (**c**), versus excitation intensity, derived from 26 compression cycles and 6 power-dependent compressions on six 4% Tm^{3+} pre-ANPs (grey), 23 compression cycles on nine 7% Tm^{3+} ANPs (teal), and 21 compression cycles on eight 15% Tm^{3+} piezochromic ANPs (purple). Different symbol shapes represent different single NPs. Each compression cycle consists of 10–1000 emission versus force data points, measured at 3 s (4% Tm^{3+}), 3 s (7% Tm^{3+}), and 3–50 s (15% Tm^{3+}) integration times. Integration times for power-dependent compressions are 3–7 s per excitation power. Error bars represent S.E.M.s, propagated from the (integrated intensity versus force – for pre-ANPs and ANPs; 800 nm / 700 nm -emission ratio versus force – for piezochromic ANPs) linear fit value standard errors; compressions consisting of a lower number of emission-versus-force data points yield larger S.E.M.s. **d**. Summary of ICP-derived doping concentrations, TEM-derived NP sizes, and force measurement NES's (mean ± standard deviation, for 3 single NPs measured at the same excitation intensity) for different sensing modalities.